Device fabrication using femtosecond laser direct write method

Tan Bo Xue

A0097610E

Supervisor: **Asst. Professor Alexander Ling**

Co-supervisor: **Dr. James A. Grieve**

Department of Physics,

National University of Singapore

Abstract

Femtosecond laser direct write has been extensively used to fabricate integrated optics devices in wide bandgap dielectric materials. Most of the groups use commercially available external amplifiers that provide high energy pulses with low repetition rate of a few kilohertz. This approach is not economical due to the high cost of external amplifiers, and the cross sections of the waveguides fabricated with high pulse energy at low repetition rate are not symmetric. We have developed an unamplified system with high repetition rate to fabricate waveguides in the bulk of dense flint glass (Schott SF11). The waveguides fabricated with this system show an obvious decrease in the cross-section asymmetry, and have a relatively high refractive index change of 0.02. This thesis reports the various degrees of freedoms in the system. The waveguides were characterised, and shown that they are single mode waveguides with high mode confinement.

Acknowledgement

I sincerely thank Assistant Professor Alexander Ling for giving me the opportunity to work in his group. He has taught me important scientific communication skills that will come a long way in my development as a scientist.

I would also like to express my gratitude to Dr. James A. Grieve for patiently guiding me through the entire project. This thesis would not be possible without his scientific direction and guidance. He helped me proofread this thesis, and gave me suggestions on the areas to improve on.

Besides my supervisors, I would also like to thank Manuel Rodrigues from the Centre of Advanced 2D Materials for helping me obtain high quality transmission microscope images of the waveguides.

Lastly, I would thank my family for their constant support and care. Without the laptop from my sister, I would not be able to complete this thesis due to the failure of my laptop.

Abbreviations

NA: Numerical aperture

CW: Continuous wave

FSR: Free spectral range

AOM: Acousto optic modulator

DPSS: Diode pumped solid-state

QWP: Quarter wave plate

HWP: Half wave plate

PBS: Polarising beam splitter

CCD: Charge coupled device

SMF: Single mode fibre

ENCS: Elliptical near-circular state

FWHM: Full width half maximum

PSW: Periodically segmented waveguides

Contents

1

Introduction

Optical experiments have traditionally been carried out with large scale bulk optics that require very precise alignment and high stability of each optical component. These alignment and stability issues pose a challenge to large scale manipulation of individual photons. For such applications, an integrated optics platform built on a network of waveguides that transmit light in a confined manner will be more advantageous. The integrated optics platform was first proposed in 1969 by S. E. Miller[1]. The technology has since been extensively used in modern communication technology to transmit information through confined transmission of light and in other fields such as quantum optics[2]. In Miller's paper, the concept of miniature lasers and modulators that will minimise the effects of thermal, mechanical and acoustic fluctuations have on the system was proposed. Optical waveguides form the basis of an integrated optics circuits just like conducting connections that form the basis of an electronic integrated circuit. Numerous methods of waveguide fabrication have been developed, including thin-film deposition, substitutional doping, carrier concentration reduction, etching and others[3]. The fabrication methods mentioned involve several stages, and the fabricated waveguides lie on a two dimensional plane.

In this project, we explore femtosecond laser direct write which is a relatively recent waveguide fabrication method that was first demonstrated in 1996 by K. Hirao et al.[4] This method enables the fabrication of three dimensional devices in wide bandgap materials. Numerous groups have demonstrated the technique in the fabrication of integrated optical devices. Most of the groups use femtosecond lasers that operate at a repetition rate of a few kilohertz with an amplifier to produce the required intensity for permanent modification of a bulk wide bandgap material. Highly energetic laser pulses with a low repetition rate of a few kilohertz produce waveguides with asymmetric geometries. Waveguides with asymmetric cross sections may not be suitable for quantum applications, where information is encoded in a two-state qubit using the degrees of freedom of a photon that includes polarisation, optical mode, path and time-bin[5]. Birefringence due to the asymmetric geometry of the waveguide might change the polarisation state of the photon. Therefore, we aim to develop a system that does not require an external amplifier and is capable of fabricating devices with minimal birefringence.

This thesis will discuss the processes of femtosecond laser direct write method that leads to permanent modification in the bulk of the material. The degrees of freedom that we have in our direct write system will be examined, and the the devices fabricated with the direct write system that we have developed were characterised.

2

Femtosecond laser direct write

Since K. Hirao et al. pioneered the use of femtosecond laser direct write method[4], different groups have used the method to fabricate integrated optic devices such as optical waveguides[4], Y-junction splitters[6], and X-couplers[7] in wide bandgap materials. The femtosecond laser direct write method enables the fabrication of three dimensional devices in the bulk of wide bandgap materials in a single process, and there is no need for lithographic mask. This technique works by focusing femtosecond laser pulses into a very small focal volume within the bulk of the material. Within the small focal volume, there may be multiphoton absorption, optical breakdown and plasma formation due to the high intensity[8].

Several parameters determine the mechanism of material modification. There are two directions in which the transparent sample can be moved relative to the laser beam, either in the direction parallel to the laser beam axis (longitudinal) or in the direction orthogonal to the direction of the laser beam axis (transverse). The longitudinal scanning direction produces waveguides with a radially symmetric cross section due to the Gaussian intensity profile of the laser beam. The transverse scanning direction produces waveguides that are elongated along the direction of the laser beam as shown in figure 2.1. Although longitudinal writing produces a radially symmetric cross section that would in principle minimise the birefringence due to the geometry, it is limited by the working distance of the objective lens used to focus the beam into the bulk of the sample. A high numerical aperture (NA) objective lens which produces a tight focus has a very short working distance of only a few hundred micrometres, hence it is not able to fabricate waveguide of arbitrary length. Scanning the sample in the direction transverse to the laser beam can overcome the limitations of longitudinal writing, enabling the fabrication of waveguides with arbitrary lengths. The asymmetry of the waveguide cross section profile caused by transverse writing can be reduced by using a high NA objective lens that has a shorter confocal parameter as shown in figure 2.1. At a high repetition rate regime, the volume of the melted glass grows radially due to thermal diffusion effects that are isotropic and tend to produce features that are more spherical. Therefore, modification of the glass with a high repetition rate laser might also help to reduce the asymmetry of the waveguide.

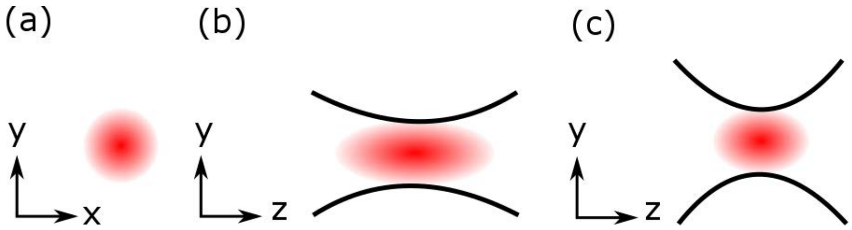

Figure 2.1: (a) Cross section intensity profile of a laser beam propagating in the z direction, (b) side intensity profile of the laser beam focused with a low NA objective lens, and (c) side intensity profile of the laser beam focused with a high NA objective lens.

2.1 Optical breakdown in the bulk of dielectric materials

Energy deposited by laser pulses in the bulk of dielectric materials can cause permanent changes to the refractive index via different mechanisms such as colour center formation, density variation and void formation[8]. There is no linear absorption of laser light in a transparent dielectric material since the bandgap of the material is higher than the photon energy of the laser light. In order to change the material permanently by optical means, the laser energy has to be absorbed by the material nonlinearly to excite the electrons from the valence band to the conduction band. There are two ways an electron can be excited nonlinearly via either photoionisation or avalanche ionisation.

In a photoionisation process, the electrons are excited directly by the laser field. Multiple photons (two or more depending on the bandgap of the material) excite a single electron from the valence band to the conduction band. There are two regimes of photoionisation, multiphoton ionisation and tunneling ionisation, that are dependent on the laser frequency and intensity[9]. Keldysh described the two regimes of photoionsation within the same framework. In his paper, an adiabatic parameter that is also known as the Keldysh parameter, γ, is defined as

$$\gamma = \frac{\omega}{e}\sqrt{\frac{mcn\epsilon_0 E_g}{I}} \tag{2.1}$$

where ω is the laser frequency, m and e are the reduced mass and charge of the electron, c is the speed of light, n is the refractive index of the material, ϵ_0 is the permitivity of free space, E_g is the bandgap of the material, and I is the intensity of the laser. At a lower light frequency, the photoionisation process is essentially a tunnelling process where the Coulomb potential between the valence electron and the atom is suppressed, thus increasing the probability of electron tunnelling across the potential wall into the conduction band. When the light frequency is higher, but not sufficiently high for single photon absorption, the photoionisation process is a multiphoton absorption process where multiple photons with total energy greater than the bandgap excite the electron into the conduction band.

Multiphoton absorption dominates the photoionisation process when the Keldysh parameter is larger than 1.5, and tunneling becomes the dominant process when the Keldysh parameter is smaller than 1.5. The rate of multiphoton absorption is given by

$$p(I) = \sigma_k I^k \tag{2.2}$$

where σ_k is the multiphoton absorption coefficient for k-photon absorption[10]. Excitation of a valence band electron to the conduction band requires a minimum number of photons k such that $k\hbar\omega \geqslant E_g$. Terms with higher k have multiphoton absorption coefficients that are orders of magnitude smaller, thus the probability of multiphoton absorption with more photons is low. This implies that multiphoton absorption has to be a high intensity phenomena.

Valence band electrons can also be excited to the conduction band through avalanche ionisation where there is free-carrier absorption that is followed by impact ionisation. Electrons that are already in the conduction band can absorb photons linearly to be excited to higher energy level. Using femtosecond direct write method, the multiphoton absorption process outlined in the previous paragraph provides the seed electrons needed for the avalanche process to initiate. After absorbing n photons linearly, where n is the smallest number that satisfies $n\hbar\omega \geqslant E_g$, the electron now has energy excess of the minimum band gap energy. This excess energy of the conduction band electron can then be transferred to an electron in the valence band through collisions, hence ionising that electron. This process creates two electrons that have energy close to the conduction band minimum, the electrons will absorb photons linearly through free-carrier absorption and subsequently excite more valence band electrons to the conduction band through impact ionisation. The avalanche process has to be sustained by the laser field. The electron density N in the conduction band grows as follows[10]

$$\frac{dN}{dt} = \eta N - \frac{N}{\tau} \tag{2.3}$$

where η is the avalanche ionisation rate, and τ is the electron lifetime, i.e. the average time for the electrons to recombine.

2.2 Ultrafast laser pulse generation

Lasers can operate in either continuous wave (CW) mode or pulsed mode. Pulsed lasers are desirable when there is a need for high peak optical power since the laser pulse has a finite duration. Laser pulses can be used in micromachining of material and nonlinear optics studies as the laser pulse can provide high intensity that is not achievable by a CW laser. There are several ways of producing laser pulse. One straightforward method is to use a CW laser in tandem with an external switch or modulator that allows periodic transmission of the light for a short duration of time. The abovementioned method is not energetically efficient because optical energy is lost when the light is blocked, and the peak power of the pulse does not exceed the peak power of the original CW laser.

There are methods to produce optical pulses more efficiently; these methods switch the laser on and off through internal modulation. Energy is stored in the resonator during off-time and released during on-time. The peak power of the optical pulses produced using these methods will be much higher than the constant power delivered by the CW laser. There are four ways to modulate the laser internally: gain switching, Q-switching, cavity dumping and mode locking[11].

Mode locking is a common method to generate ultrashort pulses. As the name of the method suggests, optical pulses are generated by locking phases of the different cavity modes of the resonator to each other. When the modes of the resonators are locked together, they form the Fourier components of a periodic function. In a laser resonator, there are many longitudinal modes that are separated spectrally by the free spectral range (FSR) $\nu_{FSR} = c/(2d)$, where d is the resonator length. In a mode-locked resonator, the complex amplitude of the mode is given by

$$A(t) = \sum_n A_n \exp\left(\frac{i2\pi n}{T_F} t\right) \tag{2.4}$$

and

$$T_F = \frac{1}{\nu_{FSR}} = \frac{2d}{c} \tag{2.5}$$

where A_n is the amplitude of the *n-th* cavity mode and T_F is the time taken for the pulse to make a round trip in the cavity.

A laser gain medium with a large lineshape function will amplify a large number of cavity modes that are contained in the lineshape function of the medium. The amplitude of each cavity mode can be treated as approximately equal due to the broad lineshape function. Thus we can write equation 2.4 as

$$A(t) = A \sum_n \left(\frac{i2\pi n}{T_F} t \right) \tag{2.6}$$

$$= A \frac{\sin(M\pi t/T_F)}{\sin(\pi t/T_F)} \tag{2.7}$$

The optical intensity is then given by

$$I(t) = |A|^2 \frac{\sin^2(M\pi t/T_F)}{\sin^2(\pi t/T_F)} \tag{2.8}$$

The number of modes $M \approxeq \Delta\nu/\nu_{FSR}$, since it is proportional to the linewidth of the gain material $\Delta\nu$. Therefore, the pulse duration $\tau_{pulse} = T_F/M \approxeq 1/\Delta\nu$. The pulse duration τ_{pulse} is inversely proportional to the atomic linewidth $\Delta\nu$ of the gain material, thus very short laser pulse can be generated by a medium with very broad atomic linewidth using the mode lock method. The peak intensity of the generated pulses will be M times the mean intensity.

The phase of the cavity modes can be locked using either active or passive modulator. A variable attenuator placed inside the oscillator modulates the transmission of the light at a frequency corresponding to the round trip time as shown in figure 2.2. With each round trip within the cavity, the modes that are in phase will be amplified and those that are out of phase will be attenuated. After several round trips, cavity modes that are in phase would be greatly amplified and those that are not in phase are greatly attenuated, thereby forming optical pulses. The peak of each pulse would be at the time of maximum transmission of the modulator[12].

Passive modulation can be achieved with a saturable absorber or Kerr-lens mode-locking. A Kerr medium, i.e. a nonlinear optical medium, changes its refractive index with the optical intensity of the light. Placing such a medium in the resonator will focus a high intensity beam with the focal length being inversely proportional to the intensity. The Kerr medium will reduce the mode cross sectional area for high intensity beam such that mode will pass through

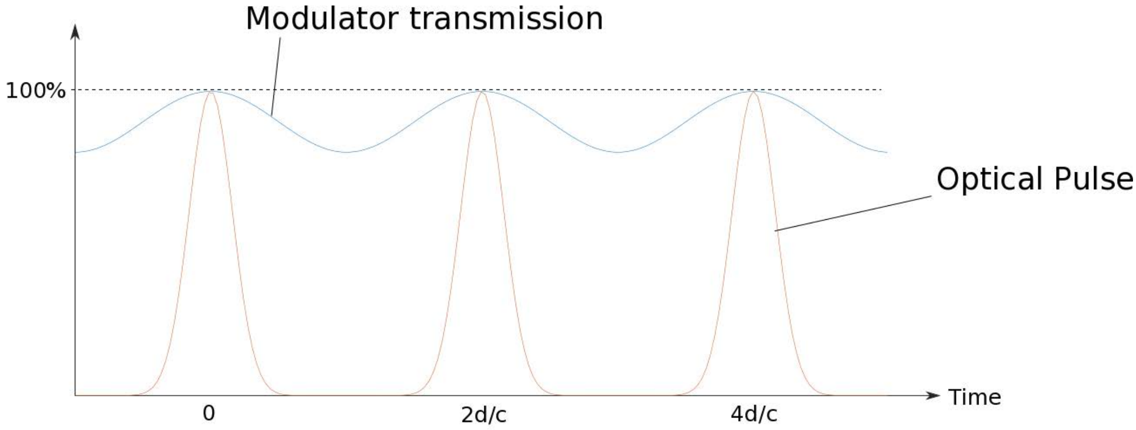

Figure 2.2: Periodic modulator transmission and mode locked optical pulses.

a correctly positioned aperture. The overlap of the cavity mode with the pump mode can be increased due to the focusing of the Kerr medium.

2.3 Laser pulse repetition rate

Permanent modification in the bulk of a wide bandgap material using femtosecond laser direct write method can be achieved at both high repetition rate regime and low repetition rate regime. The thermal diffusion time, i.e. the time it takes for the energy deposited by the laser pulse to diffuse out of the focal volume through thermal conduction, is a useful benchmark to separate the repetition rate into two regimes. At low repetition rate regime, the time between each pulse is greater than the thermal diffusion time. At high repetition rate regime, the time between each pulse is shorter than the thermal diffusion time. The damage mechanism of a high repetition rate regime is different from that of a low repetition rate regime.

With a high repetition rate, the next pulse arrives before the energy of the previous pulse is able to diffuse out of the focal volume into the surrounding lattice. Therefore, the nonlinear absorption of energy and the thermal conduction of energy to the lattice is decoupled. There is an incubation effect since the energy of many pulses is deposited in the material before it starts dissipating to the surrounding lattice through thermal conduction. The electron density continues to increase until the plasma frequency reaches the critical plasma frequency[13]. Energy dissipation to the surrounding lattice happens after the laser pulse is gone, either by turning off the laser or moving the laser beam relative to the material. The fast deposition of energy in the bulk of the material, on a time scale shorter than the thermal diffusion time, increases the temperature in the small focal volume. When the temperature exceeds the working temperature of the glass, it softens and results in densification of the material. After the temperature in the volume cools, the densification is fixed in place leading to a permanent change in morphology within the bulk. The incubation effect acts as a point source of thermal energy from which the energy dissipates radially, thus producing morphology that is more circular and less dependent on shape of the focal volume[14]. At steady state, the diameter of the modified structure would stop increasing as the rate of energy diffusing out of the volume equals the power input of the laser.

At a low repetition rate, subsequent pulse arrives after the pulse energy has diffused out of the focal volume through thermal conduction. Hence there is little accumulation of energy in the bulk of the material, and this results in a smaller region of material modification. Subsequent pulse that arrives in the bulk of the material does not increase the dimension of the structure. In order to achieve larger material modification, the pulse energy has to be amplified. However, high energy pulses that are order of magnitudes larger than the threshold intensity will result in a cone-like morphology due to the strong self-focusing of the pulse at high power. In order to produce a continuous device such as a waveguide in the bulk, there has to be significant overlap of the structures formed by individual pulse. As a result, the maximum scanning speed that can produce a smooth continuous structure is much lower than that for a high repetition rate laser writing. Therefore, using a high repetition rate laser for direct write enables a more efficient fabrication of devices.

2.4 Femtosecond laser direct write setup

Figure 2.3 shows the schematic of the experimental setup. In our setup, we have a Diode Pumped Solid-State (DPSS) laser (Verdi V10) that optically pumps the Titanium Sapphire laser (Mira 900) at 532nm. The length of the laser oscillator was extended to halve the repetition rate and increase the pulse energy. The extended laser oscillator produces optical pulses at a repetition rate of 38MHz, with a pulse duration of 160fs at 800nm. After the laser beam escapes the laser oscillator, it is modulated by a burst picker consisting of Acousto Optic Modulator (AOM) (Gooch & Housego AOM 3080-195). When the AOM is active, a fraction of the beam is diffracted. The diffracted beam is blocked by an iris diaphragm. This burst picker setup

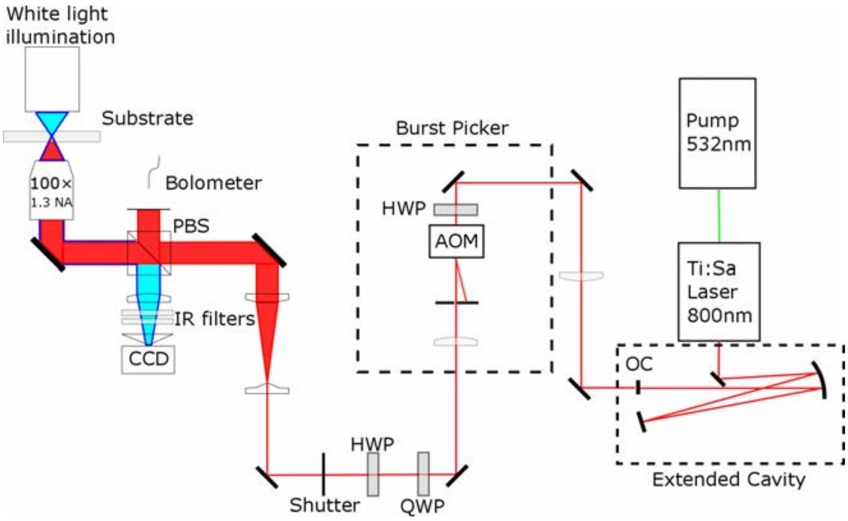

Figure 2.3: Schematic of the experimental setup. A Verdi V10 laser optically pumps the Mira 900 Ti:Sa laser at 532nm. Pumped laser oscillator and the extended cavity produce optical pulses at 800nm with a repetition rate of 38MHz and nominal pulse duration of 160fs. An AOM is included in the setup to modulate the beam and control the amount of energy that reaches the substrate without sacrificing peak power. The beam is expanded before getting focused into a small focal volume within the substrate using a 1.3NA oil immersion objective lens

allows the tuning of the energy reaching the substrate by changing the duty cycle of the signal sent to the AOM. The undiffracted beam then passes through a Quarter-Wave Plate (QWP) that converts any circularly polarised light to linear polarised light. A Half-Wave Plate (HWP) is placed after the QWP to rotate the linearly polarised light relative to the Polarising Beam Splitter (PBS) before the objective lens. Rotation of the HWP angle relative to the PBS provides another degree of freedom in the tuning energy that reaches the substrate. The laser beam is expanded and collimated using an aspheric lens and an aspheric condenser (Thorlabs ACL25416U) to fill the back aperture of the objective lens to ensure diffraction limited focusing. A 100× magnificatioin, 1.3NA oil-immersion objective lens (Nikon N100X-PFO) is used to focus the beam into the bulk of the substrate (Schott SF11). The glass substrate is secured on a computer controlled 2D linear translation stage (Alio linear motion system). Above the substrate is a white light illumination system used to image the bulk of the substrate onto a Charge Coupled Device (CCD) camera (Point Grey Research CMLN-13S2M-CS).

2.4.1 Femtosecond laser direct write procedure

The procedures to fabricate waveguides in a glass sample are as follows.

The Mira 900 Ti:Sa laser oscillator has to be aligned to optimise the output power, a bolometer was placed in the path of the output laser beam to monitor the power. The highest steady output power observed was around 1.3W at pulsed mode. However, the fabrication of the waveguides were mostly done with the output power at around 1.1W as the alignment of the oscillator deteriorates over time due to vibrations. Since 1.1W of output power is sufficient to modify the material, further alignment to restore the maximum output power is not necessary.

After the laser oscillator has been well aligned, we align the output beam with respect to the AOM to ensure maximum modulation efficiency. We switched the AOM to continuous mode during this process, and observe the brightness of the beams transmitted by the AOM. Perform the necessary alignment until the diffracted beam is at its brightest because the purpose of AOM is to diffract as much power when the signal is active. An iris aperture placed in the path of the beam after the AOM blocks the deflected beam, leaving only the undeflected beam to pass through. The efficiency of the AOM is determined by measuring the power of the beam that comes out of the AOM before and after it is switched on. The modulation efficiency achieved in our setup was determined to be around 89%, i.e. 89% of the beam is deflected when the AOM is active.

Now that the laser oscillator and the AOM have been properly aligned. The next step is to ensure that the beam that came out of the AOM is well aligned to the optical axis of the objective lens that deposits optical pulses in the bulk of the glass sample. The beam is expanded using an aspheric lens before being collimated by an aspheric condenser lens to ensure that the back aperture of the objective lens is filled by the beam to obtain a good focus.

The glass sample that used for the femtosecond laser direct write has to be cleaned thoroughly to ensure that the surface is dirt-free. This prevents any scattering of the laser beam due to the dirt particles which will in turn affect the deposition of energy in the bulk of the glass. We added generous amount of immersion oil on the surface of the glass sample before mounting it on the linear translation stage so that the oil-immersed objective lens is able to achieve greater than one numerical aperture. The glass sample and the PBS reflects a fraction of the light which is captured using a CCD camera that will be used to monitor the beam in the bulk of the glass. The height of the objective lens is controlled using computer and adjusted by a piezoelectric element with a maximum travelling distance of 200μm. By monitoring the image of the beam within the glass, we check that the beam is incident normally into the glass and not at an angle. We used the mirrors to steer the beam until the beam is normal to the surface of the glass.

With the system properly aligned, the laser can be switched back to the pulsed mode. A computer controlled shutter placed in the path of the beam is opened briefly to allow trains of laser pulse to reach the glass. With a properly aligned system, there should be observable damage in the bulk of the glass. We adjust the height of the objective lens and observe the damage at different heights; the height of the objective lens should be kept at the level where maximum damage is observed. The beam diameter in the glass should be minimised to achieve tight focusing. We adjusted the collimation of the beam before the objective lens using the aspheric lens and the aspheric condenser.

The femtosecond laser writing system is now ready to fabricate waveguides after the above-mentioned procedures have been performed. The setup contains several degrees of freedom that can be exploited to control the morphology of the waveguides. Those parameters will be discussed in greater details in the following sections.

2.5 Scanning speed

Changing the speed at which the glass sample is translated relative to the laser beam changes the amount of energy deposited in the bulk of the material. The amount of energy being deposited in a unit length can be easily obtained with the following relation

$$E = \frac{R \times E_p}{S} \tag{2.9}$$

where E is the energy deposited in the bulk per unit length of the waveguide, R is the repetition rate of the laser, E_p is the energy of each laser pulse and S is the speed at which the sample is translated relative to the beam.

2.6 Half waveplate angle

In our direct write system, we have included a QWP and a HWP after the burst picker setup to convert any circular polarised light into linear polarised light and to rotate the linear polarisation of the beam with respect to the PBS that is positioned before the oil-immersion objective lens. The PBS transmits a single linear polarisation of the laser beam and reflects the orthogonal polarisation, the transmitted power and the reflected power are measured using a bolometer. Figure 2.4 shows the percentage of the power transmitted for different angle of HWP relative to the PBS.

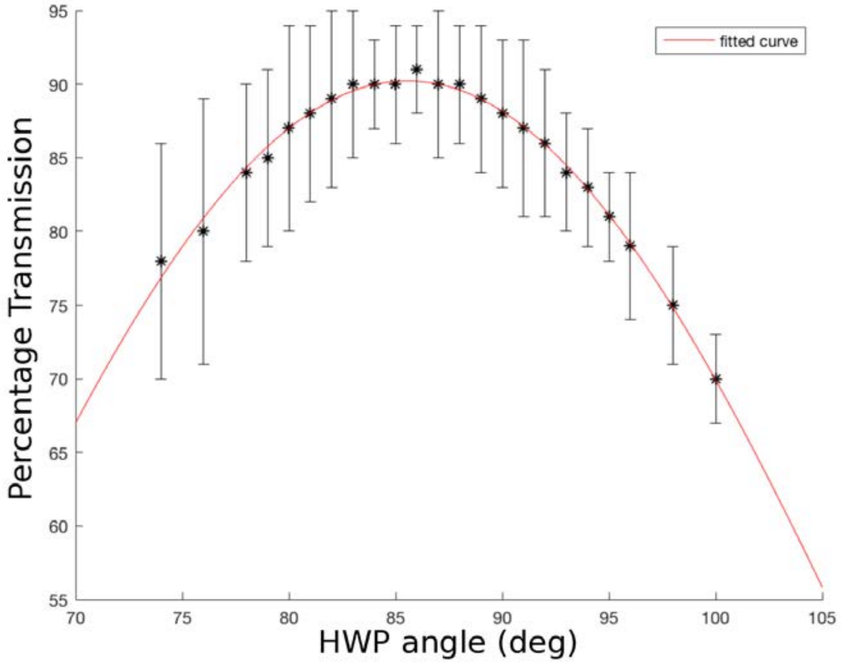

Figure 2.4: Percentage of intensity transmitted to the objective lens at different angles of the HWP relative to the PBS.

2.7 Burst picker modulation

An AOM is included in the femtosecond direct write setup to modulate the laser pulses with the aim of controlling the amount of energy that is deposited in the glass sample while preserving the peak power. In an AOM, a medium is perturbed by an acoustic wave that produces regions of compression and rarefaction. The compression (rarefaction) of the medium produces regions with higher (lower) refractive index due to changes in the density of the medium. We use a waveform generator to produce acoustic wave with amplitude A given by

$$A(x,t) = A_0 \cos(\Omega t - qx) \tag{2.10}$$

where Ω and q are the angular frequency and wavenumber of the sound wave respectively. This acoustic wave causes variation in density of the material and also changes the refractive index n of the medium as follows

$$n(x,t) = n_0 + n_1 \cos(\Omega t - qx) \tag{2.11}$$

The medium effectively becomes a dynamic graded-index medium due to the spatially periodic index profile. Even though the refractive index of the medium is dynamic, it can be treated as static since the optical frequency of light is a few orders of magnitude larger than the acoustic frequency. The sinusoidal index profile of the medium behaves like the Bragg grating, with the incoming light interferes constructively at the Bragg angle $\theta_B = \frac{\lambda}{2\Lambda}$, where λ is the wavelength of the incoming light and Λ is the periodicity of the Bragg grating. The diffracted beam will be blocked by an iris aperture so that only the undiffracted beam passes through.

A typical burst cycle is shown in figure 2.5.

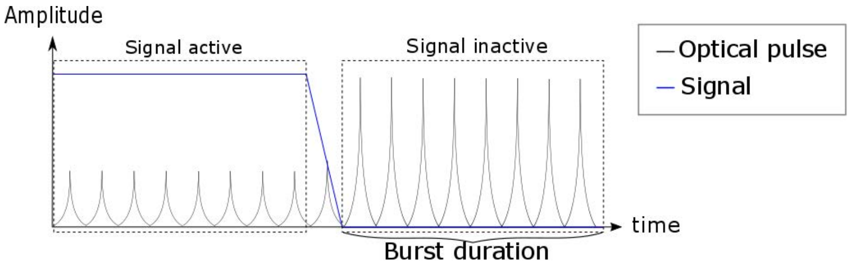

Figure 2.5: Graph showing the amplitudes of the optical pulses in a single burst cycle. Blue line shows the signal sent to the AOM, and black line shows the optical pulses. When the signal is active, the amplitude of the pulse is reduced.

The burst duration of a cycle is defined as the duration of the inactive signal as shown in the graph above. By tuning the burst duration as a fraction of the signal period, the amount of energy that reaches the substrate can be controlled. The intensity of the deflected beam can be controlled by the amplitude of the acoustic wave, i.e. deflected beam intensity increases with larger acoustic wave amplitude. We define the duty cycle as the percentage of the burst duration over the period of a single burst cycle, i.e.

$$\text{duty cycle} = \frac{\text{burst duration}}{\text{burst period}} \tag{2.12}$$

Waveguides were made with different duty cycles of the AOM ranging from 4% to 50% while keeping the scanning speed at 5mm/s, half waveplate angle relative to the PBS at 90°, and pulse energy constant at $\sim$ 20nJ. Figure 3.5 shows cross sections of waveguides made with duty cycle of 5%, 10%, 20%, 40% and 50%.

Using the method outlined in the section 3.2.1, the relation between the waveguide widths and the AOM duty cycle is studied. Figure 2.6 shows how the waveguide width changes with the duty cycle of the AOM. The graph shows the waveguide widths increasing with higher AOM duty cycle. We fit the data points of the waveguides made with 20% to 50% duty cycle linearly and included the fitted line in figure 2.6. The widths of the waveguides scale linearly with the duty cycle by 0.15μm for one percent increase in duty cycle. It is noted from figure 3.5 that the morphology of the waveguides made with duty cycles exceeding 10% is markedly different from those below 10%. There is no single consistent way of defining the waveguides' widths, hence only four of the data points were fitted linearly to demonstrate the linear relation between

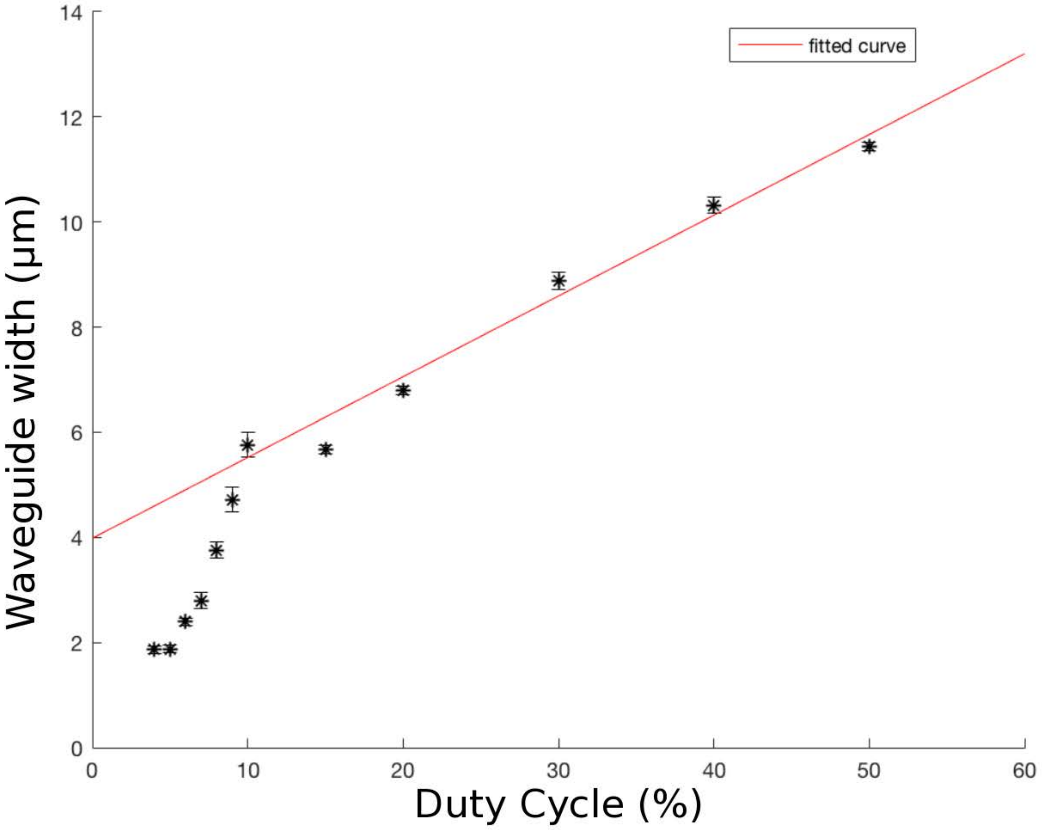

Figure 2.6: Measurement of waveguide widths fabricated with different duty cycles. The waveguides were fabricated with duty cycles ranging from 4% to 50%.

waveguide dimensions and duty cycles. Higher AOM duty cycle implies that more pulses are being reduced in amplitude in each burst cycle. Hence the energy deposited in the bulk of the glass is reduced, and the extent of material modification decreases as a consequence.

3

Waveguide characterisation

In this project, the characterisation of the waveguides was done by coupling light from a single-mode fibre (SMF) or a microscope objective lens to the waveguides. There are several methods of coupling light into waveguides which include prism coupling, grating coupling, and butt-coupling[16]. We coupled light from SMF or objective lens into the waveguides using butt-coupling method. Butt-coupling method has the advantage of in-line input and output beam, and the relative ease of handling compared to prism coupling. Prism coupling is more efficient for coupling into a film waveguide with little gap between the prism and waveguide. Hence prism coupling is not suitable for our purpose since the waveguides are in the bulk of the glass with considerable gap between the waveguide and the surface of the glass.

Butt-coupling is the most straightforward method of coupling light into the waveguides. An input mode is incident directly on the waveguide to achieve coupling. Coupling is optimised when there is maximum overlap between the input mode and the waveguide mode. Mode mismatch and Fresnel reflection loss contribute to the coupling loss. Therefore, the input beam has to be aligned to the waveguide at the correct angle to achieve minimum mode mismatch. In this project, the alignment of fibres and objective lens to the waveguides is achieved with micromanipulators (Newport ULTRAlign precision fibre optic alignment stage) that has manual actuators capable of 0.5μm and 10μm precision for fine and coarse adjustments respectively. Such high resolution actuators are required for the alignment process due to the microscopic scale of the waveguides (smallest being 1μm). Slight misalignment of even one micrometer would have drastic effect on the mode overlap and hence the coupling efficiency.

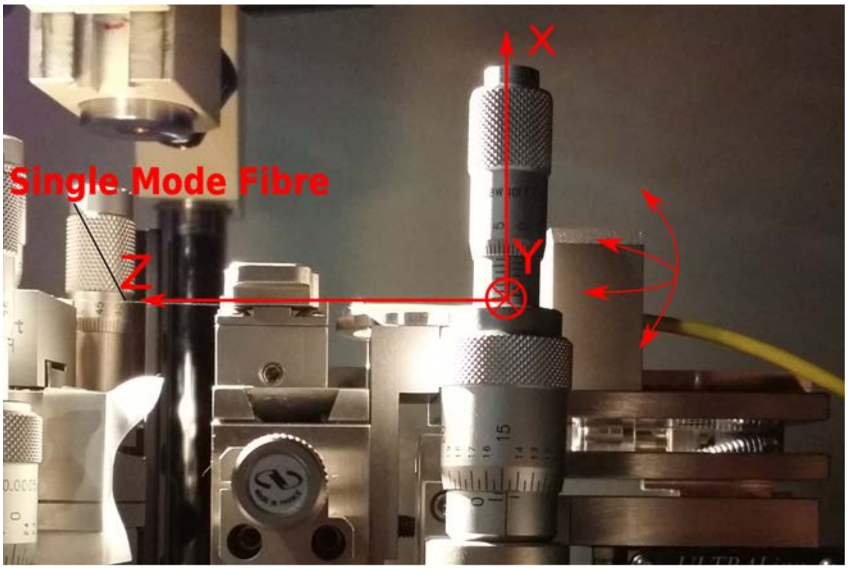

Figure 3.1: A fibre alignment stage with five degrees of freedom as shown by the red arrows. The three coordinates define the position of the fibre tip and the other two degrees of freedom being the yaw and pitch of the fibre.

Figure 3.1 shows the micromanipulator that is used to align the fibre tip to the waveguide. There are five degrees of freedom in the adjustment of the fibre that include translations of the fibre in the three orthogonal spatial coordinates, the yaw and pitch of the fibre.

3.1 Linear birefringence and diattenuation characterisation

In quantum optics, the polarisation state of a photon can be used to encode information as it defines a two-level quantum system which can be used as one of the physical implementation of a qubit, a basic unit of quantum information [17]. Therefore, it would be desirable to preserve the polarisation state of a photon. Any birefringence in the waveguide system will rotate the polarisation of the photon. There is a need to find out the birefringence of the material to determine how much the polarisation will be rotated in the *Poincaré* sphere so that we can compensate for the rotation using the appropriate combination of waveplates.

There might also be linear diattenuation in a non-isotropic material where the transmittance is different along the two orthogonal diattenuation principal axes. The transmittance is maximum along one of the axis and minimum along the orthogonal axis, so a material with linear diattenuation $D = 1$ completely blocks one polarisation component of the light and fully transmits the orthogonal component of the light. On the other hand, a material with linear diattenuation $D = 0$ transmits both components of the light equally[18]. Thus, preserving a photon's polarisation state requires minimum diattenuation in the system, since there should not be polarisation-sensitive loss. We should also characterise the diattenuation of the waveguide system so that we have the information of how the system changes the polarisation state of the photon.

The polarisation state of the light emitted from the waveguide system contains the information of the birefringence and diattenuation of the system. Therefore, we are able to determine the birefringence by measuring the complete state of polarisation of the emitted light. Stokes' parameters can be used to characterise the polarisation state of light[19]. In the Stokes vector, we have four parameters S_0, S_1, S_2 and $S3$. We defined a Cartesian coordinate system based on the H and V polarisation of a PBS, where the H and V axes are orthogonal to the direction of light propagation. The Stokes' parameters are given by the following formulas

$$S_0 = \sqrt{S_1^2 + S_2^2 + S_3^2} \tag{3.1}$$

$$S_1 = \frac{I(0^o) - I(90^o)}{I(0^o) + I(90^o)} \tag{3.2}$$

$$S_2 = \frac{I(45^o) - I(135^o)}{I(0^o) + I(90^o)} \tag{3.3}$$

$$S_3 = \frac{I_{RCP} - I_{LCP}}{I_{0^o} + I_{90^o}} \tag{3.4}$$

where $I(\phi)$ is the intensity of light polarised at an angle ϕ to the H axis, and I_{RCP} and I_{LCP} are the intensities of right-polarised and left-polarised light respectively. Each parameter has been normalised, thus varies between 1 and -1.

Any optical element can be described by a 4×4 Mueller matrix M. The Stokes vector S of the light coming out of an optical element is given by the inner product of the Mueller matrix M and the Stokes vector $\hat{S}$ of the input light as follows

$$S_c = \begin{bmatrix} S_0 \\ S_1 \\ S_2 \\ S_3 \end{bmatrix}_c = [M_{ld}][M_{lb}]\hat{S}_c = \begin{pmatrix} m_{11} & m_{12} & m_{13} & m_{14} \\ m_{21} & m_{22} & m_{23} & m_{24} \\ m_{31} & m_{32} & m_{33} & m_{34} \\ m_{41} & m_{42} & m_{43} & m_{44} \end{pmatrix} \begin{pmatrix} \hat{S}_0 \\ \hat{S}_1 \\ \hat{S}_2 \\ \hat{S}_3 \end{pmatrix} \tag{3.5}$$

where c indicates different output polarisation states (i.e. $0^o, 45^o, 90^o, 135^o$, and right-hand circular).

The Mueller matrix of a linear birefringence material can be expressed as

$$M_{lb} = \begin{pmatrix} 1 & 0 & 0 & 0 \\ 0 & \cos(4\alpha)\sin^2(\beta/2) + \cos^2(\beta/2) & \sin(4\alpha)\sin^2(\beta/2) & \sin(2\alpha)\sin(\beta) \\ 0 & \sin(4\alpha)\sin^2(\beta/2) & -\cos(4\alpha)\sin^2(\beta/2) + \cos^2(\beta/2) & -\cos(2\alpha)\sin(\beta) \\ 0 & -\sin(2\alpha)\sin(\beta) & \cos(2\alpha)\sin(\beta) & \cos(\beta) \end{pmatrix} \tag{3.6}$$

where α is the principal angle of the slow axis and β is the phase delay[20].

The Mueller matrix of a linear diattenuation material can be similarly expressed as

$$M_{ld} = \begin{pmatrix} \frac{u+v}{2} & \frac{\cos(2\theta_d)(u-v)}{2} & \frac{\sin(2\theta_d)(u-v)}{2} & 0 \\ \frac{\cos(2\theta_d)(u-v)}{2} & \frac{(\sqrt{u}+\sqrt{v})^2}{4} + \frac{\cos(4\theta_d)(\sqrt{u}-\sqrt{v})^2}{4} & \frac{\sin(4\theta_d)(\sqrt{u}-\sqrt{v})^2}{4} & 0 \\ \frac{\sin(2\theta_d)(u-v)}{2} & \frac{\sin(4\theta_d)(\sqrt{u}-\sqrt{v})^2}{4} & \frac{(\sqrt{u}+\sqrt{v})^2}{4} + \frac{\cos(4\theta_d)(\sqrt{u}-\sqrt{v})^2}{4} & 0 \\ 0 & 0 & 0 & \sqrt{uv} \end{pmatrix} \tag{3.7}$$

where θ_d is the diattenuation axis angle and u and v are the transmittances of the optical element for light that has polarisation parallel and perpendicular to the diattenuation axis respectively.

One can extract the linear birefringence properties of an optical element, i.e. α and β, from the output Stokes vector S. Three different polarisation states corresponding to the three different basis states (eigenstates of the Pauli matrices) are required at the input to obtain the linear birefringence properties. The three different input states are $\hat{S}_{0^o} = [1, 1, 0, 0]$, $\hat{S}_{45^o} = [1, 0, 1, 0]$ and $\hat{S}_{RHC} = [1, 0, 0, 1]$. The principal axis angle α and phase delay β of the linear birefrigent material are then given by[18]

$$2\alpha = \tan^{-1}\left[-\frac{S_{0^o}(S_3)}{S_{45^o}(S_3)}\right] \tag{3.8}$$

$$\beta = \tan^{-1}\left[\frac{S_{45^o}(S_3)}{\cos(2\alpha)S_{RCP}(S_3)}\right] \tag{3.9}$$

The diattenuation axis angle θ_d and the diattenuation D are given by[18]

$$2\theta_d = \tan^{-1}\left(\frac{S_{45^o}(S_2) + S_{135^o}(S_2)}{S_{0^o}(S_1) + S_{90^o}(S_1)}\right) \tag{3.10}$$

$$D = \frac{u-v}{u+v} = \frac{S_{0^o}(S_1) + S_{90^o}(S_1)}{\cos(2\theta_d)[S_{0^o}(S_0) + S_{90^o}(S_0)]} \tag{3.11}$$

where $S_{in}(S_n)$ denotes the n-th Stokes parameter for a given input S_{in}, e.g. $S_{0^\circ}(S_1)$ represents S_1 for an input polarised in the horizontal direction.

Figure 3.2 shows the experimental setup for measuring the output Stokes vectors S. The QWPs and polarisers were calibrated to ensure accurate measurement. The intensity of the output light was measured with an imaging ensemble that consists of a 40× magnification, 0.75 NA objective lens (Nikon N40X-PF) and a CCD sensor (Chameleon USB2.0 CMLN-13S2M-CS). The optical system that was examined comprised of a waveguide, an objective lens that couple light into the waveguide and another objective lens that collect the light coming out of the waveguide. The input Stokes vector $\hat{S}$ is transformed as follows

$$S = M\hat{S} \tag{3.12}$$

where the composite Mueller matrix $M = M_{obj}M_{WG}M_{obj}$. The optics of the objective lens will have an effect on the polarisation state of the light transmitted by the waveguide, and hence there is a need to determine the Mueller matrix M_{obj} of the objective lens.

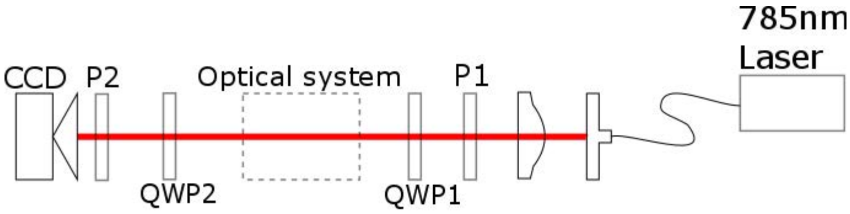

Figure 3.2: Schematic of the setup to measure the Stokes parameter of an optical system. The optical system to be examined is incident with a 785nm beam with the polarisation state controlled by the polariser P1 and the QWP1. The state of the output light is determined with a combination of polariser P2, QWP2 and a CCD camera.

One is able to obtain the Mueller matrix from the output Stokes vector measurement using equation 2.13 as follow

$$\begin{bmatrix} S_{0^o} \\ S_{90^o} \\ S_{45^o} \\ S_{RCP} \end{bmatrix}_i = \begin{bmatrix} \hat{S}_0(0^o) & \hat{S}_1(0^o) & \hat{S}_2(0^o) & \hat{S}_3(0^o) \\ \hat{S}_0(90^o) & \hat{S}_1(90^o) & \hat{S}_2(90^o) & \hat{S}_3(90^o) \\ \hat{S}_0(45^o) & \hat{S}_1(45^o) & \hat{S}_2(45^o) & \hat{S}_3(45^o) \\ \hat{S}_0(RCP) & \hat{S}_1(RCP) & \hat{S}_2(RCP) & \hat{S}_3(RCP) \end{bmatrix} \begin{bmatrix} M_{(i+1)1} \\ M_{(i+1)2} \\ M_{(i+1)3} \\ M_{(i+1)4} \end{bmatrix} \tag{3.13}$$

where $[S_{input}]_i$ is the i-th Stokes parameter for a given input state and the M vector contains the elements of the Mueller matrix for that optical element.

The Mueller matrix of the objective lens that image the waveguide was measured to be

$$M_{obj} = \begin{pmatrix} 0.992 & 0.004 & -0.025 & -0.014 \\ 0.004 & 0.992 & -0.098 & -0.022 \\ -0.005 & 0.024 & 0.964 & -0.009 \\ 0.017 & 0.018 & -0.093 & 0.995 \end{pmatrix} \tag{3.14}$$

It is difficult to have input states that are purely circularly polarised because of the imperfections of the QWP. R.M.A. Azzam et al. came up with a scheme to overcome the problem[21]. With an imperfect QWP, it is impossible to create exact RCP or LCP states. Instead, an imperfect QWP will create elliptical near-circular state (ENCS) with the Stokes vector given by[22]

$$\hat{S} = [1 \quad \cos(2\epsilon)\cos(2\theta) \quad \cos(2\epsilon)\sin(2\theta) \quad \sin(2\theta)]^t \tag{3.15}$$

where ϵ and θ are the ellipticity angle and major axis angle respectively. A small parameter

$$\beta = 45^o - |\epsilon| \tag{3.16}$$

is introduced to represent the deviation of the ENCS from exact circular polarised states. The Stokes vector of a right-handed ENCS is then expressed in terms of β and θ as follow

$$\hat{S}_{ENCS}(\theta) \approx [1 \quad 2\beta\cos(2\theta) \quad 2\beta\sin(2\theta) \quad 1]^t \tag{3.17}$$

which is obtained from equation 2.15 and 2.16 using small β approximation.

Rotating the QWP and the polariser together by an angle of 90^o will produce an ENCS with perpendicular major axis angle $\theta + 90^o$. The Stokes vector of this rotated ENCS is given by

$$\hat{S}_{ENCS}(\theta + 90^o) = [1 \quad -2\beta\cos(2\theta) \quad -2\beta\sin(2\theta) \quad 1]^t \tag{3.18}$$

By measuring the responses of the system to the two ENCS states, and taking the average of the responses, we get

$$\begin{aligned} S_{av} &= [S_{ENCS}(\theta) + S_{ENCS}(\theta + 90^o)]/2 \\ &= [M\hat{S}_{ENCS}(\theta) + M\hat{S}_{ENCS}(\theta + 90^o)]/2 \\ &= M[\hat{S}_{ENCS}(\theta) + \hat{S}_{ENCS}(\theta + 90^o)]/2 \end{aligned} \tag{3.19}$$

where M is the Mueller matrix of the system and $\hat{S}_{ENCS}$ is the input Stokes vector. From

	QWP
Principal axis angle α (°)	24.29±0.06
Phase retardance β (°)	89.2±0.1
Diattenuation axis angle θ_d (°)	12 ± 2
Diattenuation D	0.030±0.002

Table 3.1: This table contains the principal angle of the slow axis (deg.), the phase delay (deg.), the diattenuation angle (deg.) and the diattenuation parameters of the QWP.

equation (2.18) and (2.19), we have

$$[\hat{S}_{ENCS}(\theta) + \hat{S}_{ENCS}(\theta + 90^o)]/2 = [1\,0\,0\,1]^t \tag{3.20}$$

$$= \hat{S}_{RCP} \tag{3.21}$$

which is the Stokes vector of a RCP state.

Therefore, this scheme allows us to find the output Stokes vector of a system for an unattainable exact circularly polarised state by evaluating the average of the two output Stokes vector for an input ENCS state and the orthogonal state.

The linear birefringence and diattenuation properties of a QWP were measured to verify the method described above. Table 3.1 gives the principal axis angle (α), the phase delay (β), the diattenuation angle (θ_d), and the diattenuation (D) of the QWP.

The phase delay angle values that we see in table 3.1 do not agree with what are expected of a zero-order QWP (90°). However, it has to be noted that the wavelength of the input light (785nm) is not the same as the design wavelength of the waveplates (780nm).

The Mueller matrices for the zero-order QWP was evaluated and given as follows

$$M_{QWP} = \begin{pmatrix} 0.981 & -0.035 & 0.028 & 0.022 \\ 0.024 & 0.419 & -0.508 & -0.817 \\ 0.007 & -0.504 & 0.520 & -0.720 \\ -0.041 & 0.774 & 0.656 & 0.098 \end{pmatrix} \tag{3.22}$$

Principal axis angle α (°)	1.5±0.2
Phase retardance β (°)	73.0±0.2
Diattenuation axis angle θ_d (°)	45 ± 1
Diattenuation D	0.3±0.1

Table 3.2: This table contains the principal angle of the slow axis (deg.), the phase delay (deg.), the diattenuation angle (deg.) and the diattenuation parameters of the waveguide made with 10% duty cycle and 5mm/s scanning speed.

$$M_{\text{Waveguide}} = \begin{pmatrix} 1.023 & -0.003 & -0.039 & 0.111 \\ -0.001 & 1.017 & 0.236 & -0.017 \\ -0.001 & 0.210 & -0.365 & -0.868 \\ -0.024 & 0.088 & -0.874 & -0.230 \end{pmatrix} \tag{3.23}$$

Table 3.2 shows the principal axis angle (α), the phase delay (β), the diattenuation angle (θ_d), and the diattenuation (D) of a waveguide fabricated with 10% duty cycle and 5mm/s scanning speed. The Mueller matrix for the same waveguide is given by equation 3.23. The birefringence of the waveguide is substantial, with a relative phase delay of 73.0°. Meanwhile the diattenuation of the waveguide was determined to be 0.3 ± 0.1, and this implies the polarisation along one axis is attenuated more than the orthogonal polarisation. Polarisation state of a photon is not preserved because of the diattenuation in the waveguide. This implies that despite the symmetric geometry of the waveguide, it is not suitable for applications where information is encoded in the polarisation.

3.2 Waveguide morphology study

There are several ways to study the morphology of the waveguides made with the femtosecond direct write method. Optical microscopy, scanning electron microscopy and refractive index profiling can be used to investigate the morphology of the waveguides.

3.2.1 Optical microscopy

Images of the waveguides were obtained using polarising imaging method. We used a Nikon Eclipse LV100ND microscope that was fitted with a Nikon LV-P0 polariser. The polarisation imaging method is a common method used to determine the internal stress in a transparent dielectric material. A transparent material may exhibit birefringence properties when there is built up stress in the material. The birefringence property of the material rotates polarised light. As a result, when one views the material illuminated with a polarised light source through a polariser, non-uniform colour and intensity distribution will be observed. A linearly polarised white light source will be rotated non-uniformly by the transparent material, with the amount of rotation dependent on the birefringence of the material and the spectrum of the light source. Different wavelengths experience different relative phase retardation between two orthogonal directions along the principal birefringent axes.$\Delta\delta$ given as follow

$$\Delta\delta = \frac{2\pi\Delta n}{\lambda_0}L \tag{3.24}$$

where δn is the birefringence of the material, L is the thickness of the material, and λ_0 is the wavelength of the light source in vacuum.

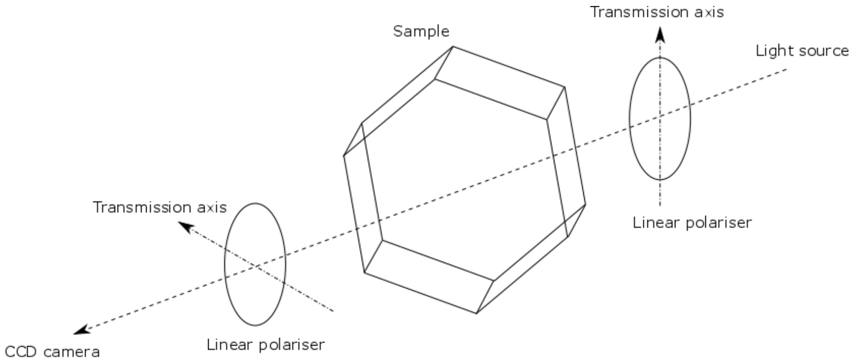

Figure 3.3: Monochromatic or white light source illumination is linearly polarised before incident on the sample. The sample will rotate the polarised light, another linear polariser is placed after the sample with the transmission axis normal to the first polariser to transmit light polarised along the original polarisation. A CCD camera is placed at the end of the setup to capture the image.

Figure 3.3 shows the schematic of a simple setup for polarisation imaging. A monochromatic or white light source is linearly polarised with a linear polariser. The birefringence in the material rotates the incident linearly polarised light. Placing another linear polariser after the sample with the transmission axis orthogonal to the first polariser will block the transmission of light polarised in the same direction as the first polariser and transmit any light polarised in the orthogonal direction.

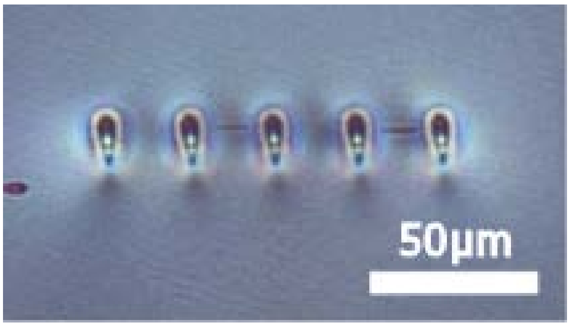

Figure 3.4: Bright field image of a cluster of five waveguides obtained using cross-polarisation imaging method. The waveguides were made with a 1300kHz burst rate, active burst duration of 0.4μs, and scanning speed of 5mm/s.

Figure 3.4 shows a bright field image of a cluster of five waveguides obtained with cross-polarisation imaging method. The waveguides were made with a duty cycle of 48%, and are spaced 25μm apart.

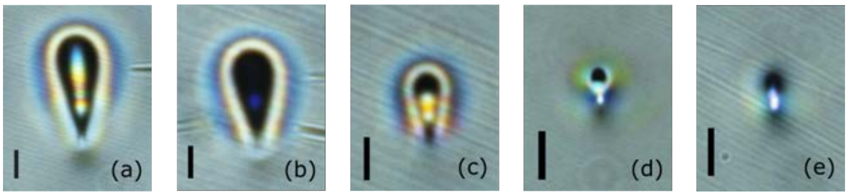

Figure 3.5: Cross sections of waveguides seen under transmission optical microscope. Waveguides (a),(b),(c),(d),(e) were written with duty cycle of 50%, 40%, 20%,10% and 5% respectively. All the waveguides were written with scanning speed of 5mm/s. Scale bars in the figure represent 5μm.

Figure 3.5 shows the cross sections of the waveguides made with different fabrication parameters. It is noted that the larger waveguides (a),(b), and (c) have a inverted tear-drop shape. The laser pulses were incident from the top of the figure. The asymmetric shape of the waveguide is expected because of the transverse writing scheme. Waveguides (a)-(c) have very distinct layers consisting of a central core within a dark cladding that is in turn surrounded by an bright outer ring as seen from figure 3.5 and also from figure 3.8.The waveguides shown in figure 3.5 have very different morphologies as the duty cycle changes. The waveguides made with lower duty cycle has a smaller dark region that does not envelop the bright core but lies above it, the bright outer ring is still visible.

The bright field images of two waveguides made with duty cycles of 10% and 30% were shown in figure 3.6 and 3.7 respectively. The bright field image of the waveguide shown in figure 3.7 does not have a core, and the waveguide mode shows a ring of high intensity pixels that are consistent with the bright outer ring that we observe in the bright field image. We observe changing waveguide mode when there is offset in the position of the input mode, indicating the mode guided by the bright outer ring is not single mode. Figure 3.6 shows a waveguide with a very bright core that is slightly elongated; the coupled mode of the waveguide is approximately Gaussian elongated along the vertical axis. The full width half maximum (FWHM) of the mode along the horizontal axis is 1.2μm, that is consistent with the width of the bright core in the bright field image, indicating that the mode observed is guided by the core. However, we observed that slight offset of the input beam will cause the bright region around the core to be excited and light is no longer observed in the core region. This suggests that the bright region around the core has a significantly higher numerical aperture than the core, thus a slight offset of the input causes the input mode to couple into the surrounding region instead of the core.

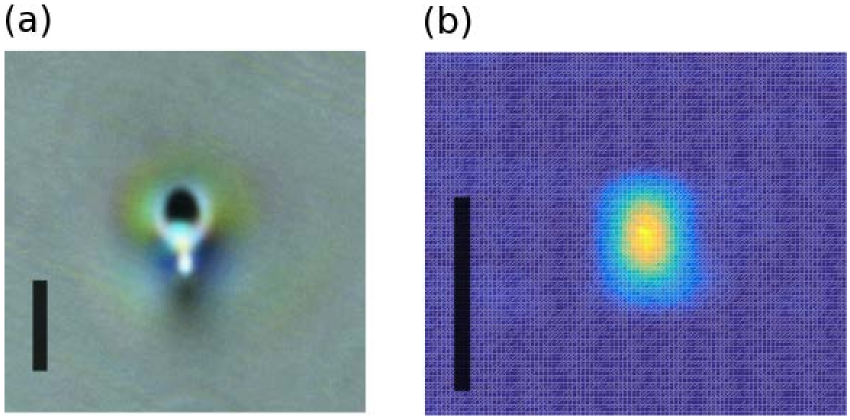

Figure 3.6: (a) Bright field image of a waveguide fabricated with 10% duty cycle, 200kHz burst rate and 5mm/s scanning speed. (b) Mode field profile at 785nm. Scale bar in the figure represent 5μm.

Figure 3.8 shows the intensity plot of figure 3.5(a) by extracting a row of the pixel values from the image. With the intensity plot, we can define the dimension of the structure based on the extremal points on the plot. This method is used in other sections of this report to determine the width of the waveguide.

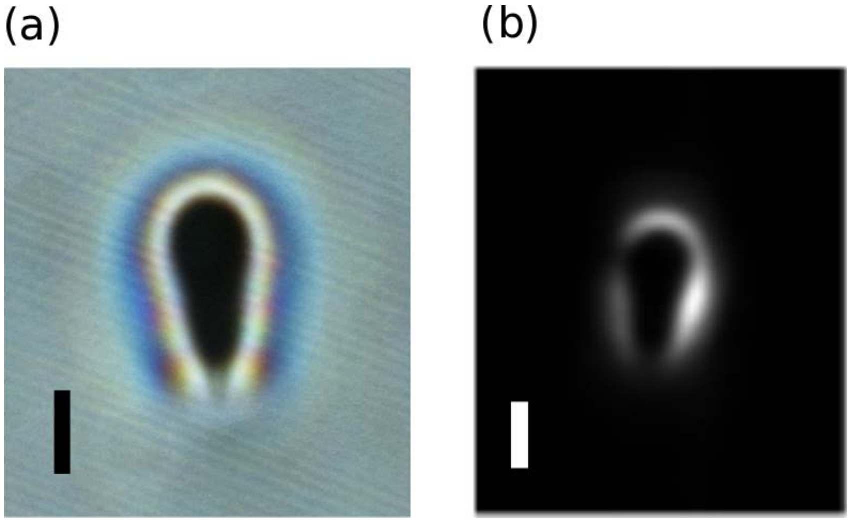

Figure 3.7: (a) Bright field image of a waveguide fabricated with 30% duty cycle, 600kHz burst rate and 5mm/s scanning speed. (b) Mode field profile at 730nm. Scale bar in the figure represents 5μm.

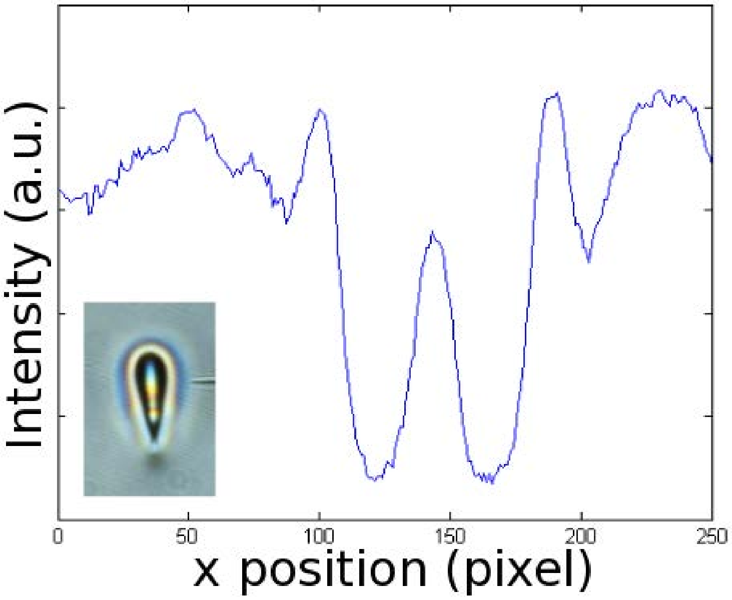

Figure 3.8: Plot of the intensity at different pixels along a line taken from Figure 3.5(a).

3.2.2 Refractive index profile

Refractive index profiles of the waveguides in the bulk of the dielectric material can be obtained in several ways. Interferometric techniques[23][24], index reconstruction from the distribution of effective index[25], and reconstruction of the index profile from the measured distribution of the guided mode[26] are several approaches to obtain the index profiles of the waveguides. In this project, we chose to reconstruct the index profiles of the waveguides' cross section from the guided mode profile. An unknown index profile of a waveguide can be reconstructed from the measured intensity distribution of the guided mode using an inverse algorithm that shall be described in detail.

The index profile n of a waveguide is given by the sum of the substrate index n_s and the index difference Δn, $n = n_s + \Delta n$. The index difference Δn is small relative to the substrate index n_s due to the weak confinement of the mode, thus

$$n^2 = (n_s + \Delta n)^2 \approx n_s^2 + 2n_s\Delta n. \tag{3.25}$$

Given the Helmholtz equation,

$$\nabla^2 E + k_0^2(n^2 - n_{\text{eff}}^2)E = 0 \tag{3.26}$$

and the small index difference approximation, the refractive index profile can be determined from an inverse algorithm,

$$\Delta n \approxeq -\frac{1}{2k_0^2 n_s}\frac{\nabla^2 E}{E} + \Delta n_{\text{eff}} \tag{3.27}$$

where $\Delta n_{\text{eff}} = n_{\text{eff}} - n_s$ is defined as the effective index difference and k_0 is the free space wavenumber.

Using the finite difference method, the index difference at each spatial coordinate can be computed from the measured intensity distribution as follows

$$\begin{aligned}\Delta n(i,j) - \Delta n_{eff} = &-\frac{1}{2n_s k_0^2 A(i,j)}[\frac{A(i+1,j) + A(i-1,j) - 2A(i,j)}{dx^2} \\ &+ \frac{A(i,j+1) + A(i,j-1) - 2A(i,j)}{dy^2}]\end{aligned} \tag{3.28}$$

where $A(i,j) = \frac{\sqrt{I(i,j)}}{I_{\max}}$ is the normalised amplitude of the intensity distribution I.

Any noise in the image of the coupled mode will affect the quality of the reconstructed index profile due to the second order derivatives in equation 3.26. Therefore, we collected one thousand mode images at 16-bit, and we averaged the images to obtain data with less noise. Figure 3.9 shows the near field mode profile of a waveguide made with 200kHz burst rate after averaging.

The index difference profile of the waveguide (figure 3.10) was obtained by applying equation 3.29 on the near field mode profile data shown in figure 3.9. It is evident from figure 3.10 that

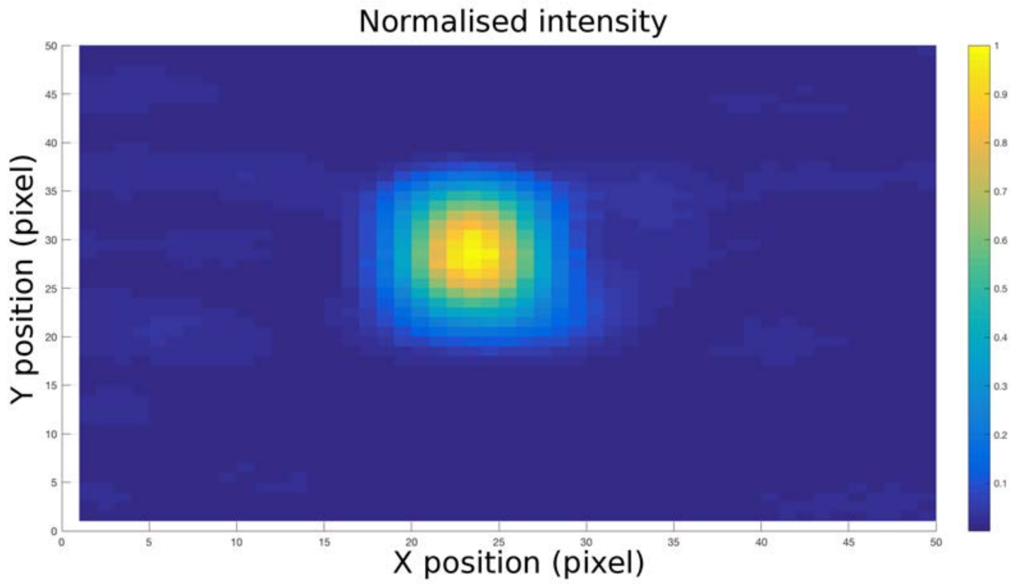

Figure 3.9: Near field mode profile of a waveguide at 785nm (written with 200kHz burst rate). The intensity has been normalised.

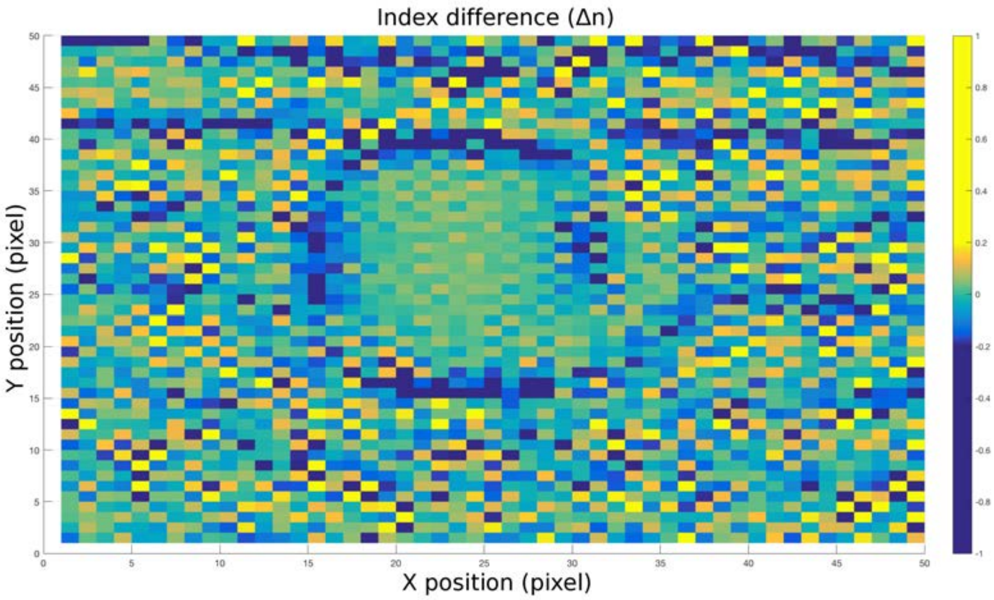

Figure 3.10: Index difference profile of the waveguide obtained using index reconstruction from guided mode. No filter is applied.

the index difference profile is still very noisy despite averaging over a thousand images. A low pass Gaussian filter,

$$H(x,y) = e^{\frac{-(x^2+y^2)}{2\sigma^2}} \tag{3.29}$$

where x and y are the index of the pixel and σ is the spread of the Gaussian filter, is subsequently applied on the averaged near field mode profile to smooth out any noise that has high spatial frequency. Figure 3.11 shows the index difference profile after a Gaussian filter of 21×21 pixels and $\sigma = 3$ is applied on the averaged near field mode profile. It is apparent that the noise in the reconstructed index difference profile has been greatly reduced. The FWHM of the index difference along the horizontal axis is 1.7μm, and that is consistent with the dimension of the core that is seen in the bright field image of the waveguide shown in figure 3.6(a), indicating that the mode is guided through the core and not other region of the waveguide. The index difference obtained using this method is around 0.02. This is higher than the index change reported by other groups[14, 27, 28]. This high index refractive index change makes the waveguide highly confining.

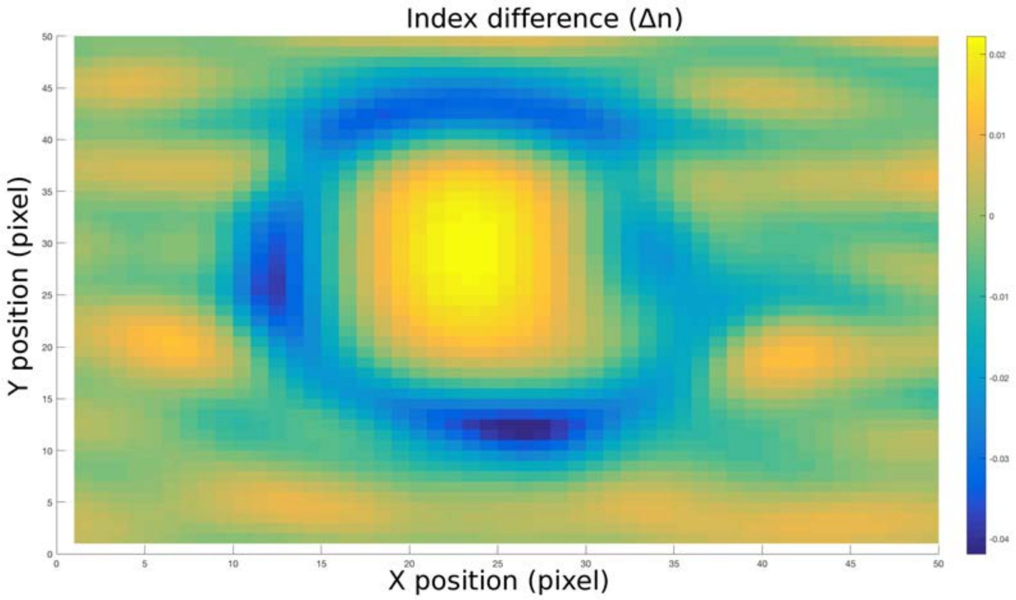

Figure 3.11: Index profile of the waveguide obtained using index reconstruction from guided mode. A Gaussian filter with $\sigma = 3$ is applied on the averaged guided mode data.

3.3 Discrete diffraction in 1D waveguide array

An integrated optic chip consists of more than just linear waveguides, other optical devices such as beam splitters and directional couplers might also be needed for applications such as interferometry. Devices such as beam splitter and directional coupler are based on evanescent coupling between the arms of waveguides. Therefore, it is important that the waveguides fabricated with our system is able to couple with each other. We investigate the evanescent coupling of the waveguides by fabricating an array of them with variable separations between each waveguide.

There is weak coupling in a waveguide array due to overlap between the fundamental modes of adjacent waveguides. Coupled mode theory can be used to study the exchange of energy between waveguides that are weakly coupled. In coupled mode theory, the transverse intensity distribution is assumed to be unchanged. In a one-dimensional waveguide array that consists of $2N + 1$ waveguides, the mode amplitude a of each waveguide is given by its corresponding coupled first-order differential equation as follow

$$\frac{da_N}{dz} = -iC_{N-1,N}\exp(i\Delta\beta z)a_{N-1} \tag{3.30}$$

$$\frac{da_j}{dz} = -iC_{j+1,n}\exp(i\Delta\beta z)a_{j+1} - iC_{j-1,n}\exp(i\Delta\beta z)a_{j-1} \tag{3.31}$$

$$\frac{da_{-N}}{dz} = -iC_{-N+1,-N}\exp(i\Delta\beta z)a_{-N+1} \tag{3.32}$$

where

$$\Delta\beta = \beta_n - \beta_{n-1} \tag{3.33}$$

is the phase mismatch per unit length and

$$\begin{aligned} C_{j+1,j} &= \frac{1}{2}(n_{j+1}^2 - n^2)\frac{k_0^2}{\beta_j}\int u_j(y)u_{j+1}(y)dy, \\ C_{j,j+1} &= \frac{1}{2}(n_j^2 - n^2)\frac{k_0^2}{\beta_{j+1}}\int u_{j+1}(y)u_j(y)dy \end{aligned} \tag{3.34}$$

are the coupling coefficients between the j-th and *(j+1)*-th waveguides. In an array of identical waveguides, the coupled first-order differential equations simplify to

$$\frac{da_N}{dz} = -iC_{N-1,N}a_{N-1} \tag{3.35}$$

$$\frac{da_j}{dz} = -iC_{j+1,n}a_{j+1} - iC_{j-1,n}a_{j-1} \tag{3.36}$$

$$\frac{da_{-N}}{dz} = -iC_{-N+1,-N}a_{-N+1} \tag{3.37}$$

and the coupling coefficients $C_{j+1,j} = C_{j,j+1} = C$ because the propagation constants of identical waveguides are equal.

The system of first-order differential equations can be solved analytically for small N, but it will be increasingly cumbersome to solve the equations as N gets larger. We can solve the set of differential equations using linear algebra,

$$\vec{a'} = -iCA\vec{a} \tag{3.38}$$

where A is a $(2N+1)\times(2N+1)$ matrix. The solution for equation (2.36) is given by

$$\vec{a} = \sum_{j=-N}^{N} k_j \vec{\eta_j} e^{r_j z} \tag{3.39}$$

where $\vec{\eta_j}$ and r_j are the eigenvector and corresponding eigenvalue of $-iCA$.

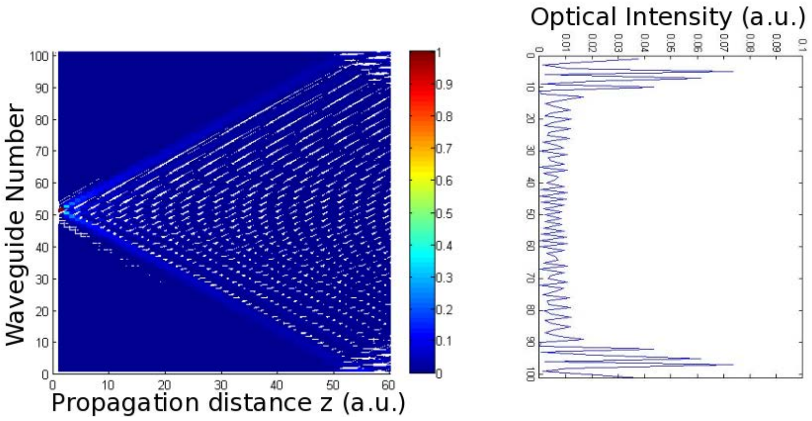

Figure 3.12: Output intensity and simulated mode propagation shown for input at the centre waveguide. It is assumed that the input mode is sufficiently small such that it is only coupled into the centre waveguide.

Figure 3.12 shows the simulated beam propagation in a linear array of 101 waveguides with the light input at the centre waveguide and the output intensity. It is noted that unlike diffraction in a continuous medium, the energy is largely contained within the two outer lobes. This phenomena is known as *discrete diffraction*.

We can observe discrete diffraction in a linear waveguide array by either measuring the output intensity at different propagation distance z or observing the propagation directly with fluorescence imaging.

Figure 3.13 shows the measured intensity distribution of an array of 21 waveguides spaced 5μm apart. One of the waveguide was excited with a narrow beam input from a SMF, and the excitation of other waveguide modes adjacent to the initial site shows evanescent coupling between the waveguides. Different sites were excited and the output intensity distributions were captured and shown in figure 3.14.

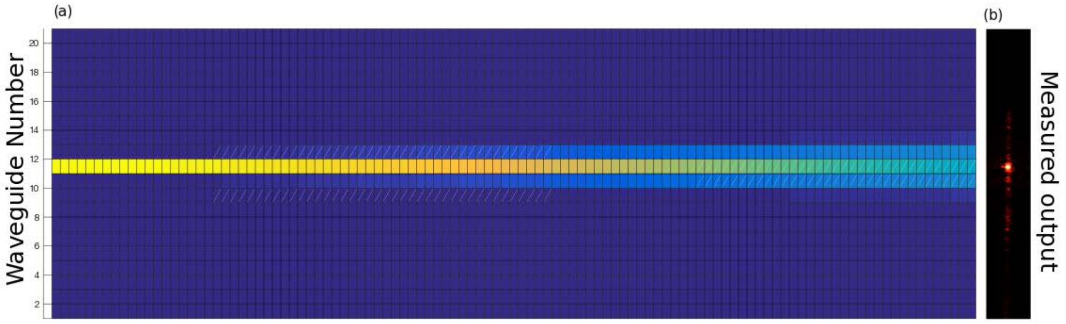

Figure 3.13: (a) A numerical simulation of a waveguide array consisting of 21 waveguides. (b) Measured output of the intensity distribution of an array of 21 waveguides spaced 5μm apart at 630nm.

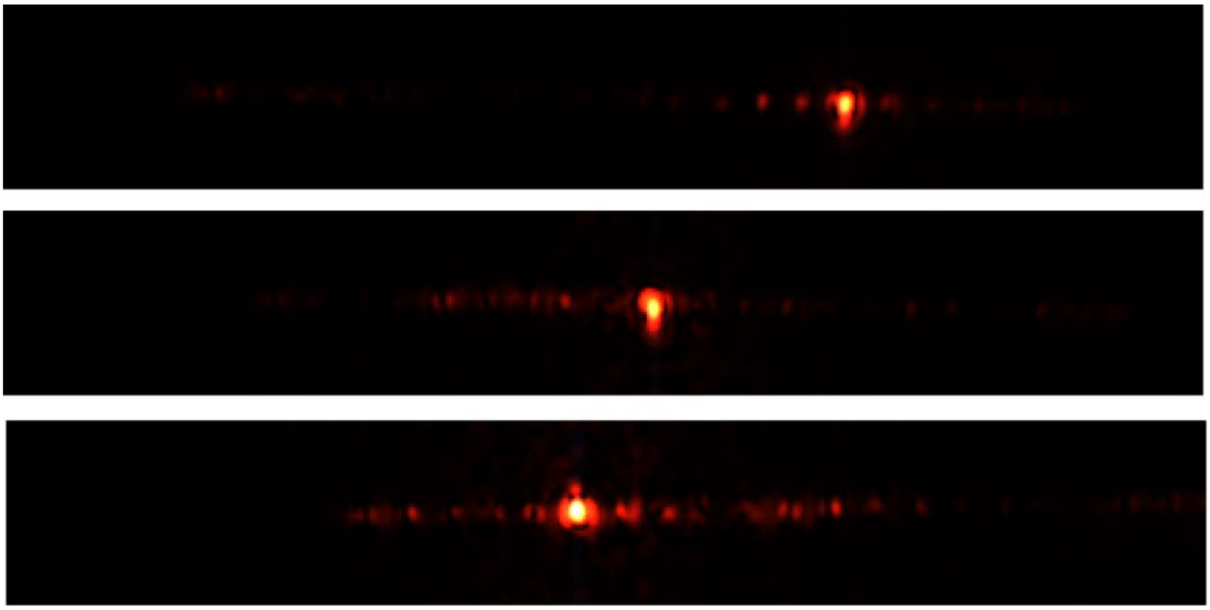

Figure 3.14: The linear array of 21 waveguides spaced 5μm apart being excited with a narrow beam input at different sites.

4

Conclusion

We have demonstrated the possibility of fabricating waveguides within the bulk of dense flint glass (Schott SF11) without the use of a commercial amplifier. This is made possible by increasing the laser cavity length in our setup to increase the pulse energy. By operating at a high repetition rate, we are able to permanently modify the material at relative low pulse energy hence allowing us to fabricate waveguides without the use of an amplifier. The scanning speed can be increased while ensuring the fabricated waveguide remains continuous; this is not possible with a low repetition rate high pulse energy system. The use of a high NA oil immersion objective lens together with increased pulse energy from an extended laser oscillator enables us to achieve intensity greater than the threshold required to cause permanent modification in bulk of the glass.

In our setup, we have included various components that gave us additional degree of freedoms in tuning of the pulse energy and the average deposited energy. The inclusion of a burst picker allows us to effectively reduce the amount of energy deposited per unit length of the waveguide fabricated while preserving the peak power of optical pulses. Figure 2.6 illustrates the effectiveness of burst picker modulation in controlling waveguide dimension. The speed at which the sample is scanned relative to the laser beam also determine the amount of energy deposited in the waveguide per unit length.

4.1 Future Work

With a high index change of around 0.02, it is possible to fabricate devices with bends due to the high mode confinement. This will open up the possibilities of fabricating devices such as directional couplers and beam splitters in a glass chip. We can also look into the possibility of fabricating periodically segmented waveguides (PSW) with variable duty cycle through modulation or slow shutter. Integrating PSW into the waveguide network in the glass would provide taper for the single mode waveguides and make coupling from fibre more efficient due to improved mode matching[29].

More work should also be done to better characterise the evanescent coupling between the waveguides. A better understanding of the evanescent coupling properties of our waveguides is needed to fabricate functional devices such as directional couplers. The smallest bending radius of the waveguides such that the waveguide mode remain confined should also be investigated.

Bibliography

[1] S. E. Miller, *Integrated Optics: An Introduction*, The Bell System Technical Journal, September 1969

[2] G. D. Marshall, A. Politi, J. C. F. Matthews, P. Dekker, M. Ams, M. J. Withford, and Jeremy L. O'Brien *Laser written waveguide photonic quantum circuits*, Optics Express, Vol. 17, No. 15, 20 July 2009

[3] R. G. Hunsperger, *Integrated Optics: Theory and Technologies*, Springer, Chapter 4, 2009

[4] K. M. Davis, K. Miura, N. Sugimoto, and K. Hirao, *Writing waveguides in glass with a femtosecond laser* Optics Letter, Vol. 21, No. 21, November 1, 1996

[5] M. A. Nielsen and I. L. Chuang, *Quantum Computation and Quantum Information*, Cambridge University Press, 2000

[6] D. Homoelle, S. Wielandy, A. Gaeta, N. F. Borelli, and C. Smith, *Infrared photosensitivity in silica glasses exposed to femtosecond laser pulses*, Optical Letter, Vol. 24, September 1999

[7] K. Minoshima, A. M. Kowalevicz, I. Hartl, E. P. Ippen, and J. G. Fujimoto, *Photonic device fabrication in glass by use of nonlinear materials processing with a femtosecond laser oscillator*, Optical Letter, Vol. 26, October 2001

[8] Matthias Will, Stefan Nolte, Boris N. Chichkov, and Andreas Tünnermann *Optical properties of waveguides fabricated in fused silica by femtosecond laser pulses*, Applied Optics, Vol. 41, No. 21, 20 July 2002

[9] L.V. Keldysh, *Ionization in the field of a strong electromagnetic wave*, J. Exptl. Theoret. Phys. (U.S.S.R.) 47, 1945-1957 (November, 1964)

[10] S.C. Jones, P.Braunlich, R.T. Casper, X.-A. Shen, and P. Kelly, *Recent progress on laser-induced modifications and intrinsic bulk damage of wide-gap optical materials*, Optical Engineering, October 1989, Vol. 28 No. 10

[11] Bahaa E. A. Saleh and Malvin Carl Teich, *Fundamentals of Photonics*, 1991 John Wiley & Sons, Inc.

[12] Andrew M. Weiner, *Ultrafast Optics*, 2009 John Wiley & Sons, Inc.

[13] B. C. Stuart, M. D. Feit, S. Herman, A. M. Rubenchik, B. W. Shore, and M. D. Perry, *Nanosecond-to-femtosecond laser-induced breakdown in dielectrics*, Phys. Rev. B, Vol. 53, 15 January 1996

[14] Shane M. Eaton, Haibin Zhang, Peter R. Herman, Fumiyo Yoshino, Lawrence Shah, James Bovatsek, and Alan Y. Arai, *Heat accumulation effects in femtosecond laserwritten waveguides with variable repetition rate*, Optics Express, Vol. 13 No. 12, 13 June 2005

[15] Russell A . Chipman, "Chapter 22: Polarimetry", *Handbook of Optics*, McGraw-Hill, 2001

[16] E. Voges, "Coupling techniques: Prism-, Grating- and Endfire-Coupling" *Integrated Optics Physics and Applications*, Ed. S. Martellucci and A.N. Chester, Springer US, Vol. 91, 1983

[17] Le Bellac, Michel, *A Short Introduction to Quantum Information and Quantum Computation*, 1st ed. Cambridge: Cambridge University Press, 2006.

[18] P. C. Chen and Y. L. Lo *Using polarimeter and Stokes parameters for measuring linear birefringence and diattenuation properties of optical samples*, EPJ Web of Conferences 6, 32001 (2010)

[19] G. G. Stokes *Trans. Camb. Phil. Soc. 9*, 399 (1852)

[20] I. C. Khoo and F. Simoni, *Physics of Liquid Crystalline Materials*, Gorden and Breach Science Publishers, 1991, Chap. 13.

[21] R. M. A. Azzam and Ali G. Lopez, *Accurate calibration of the four-detector photopolarimeter with imperfect polarizing optical elements*, Vol. 6, No. 10/October 1989/J. Opt. Soc. Am. A

[22] R. M. A. Azzam and N. M. Bashara, *Ellipsometry and Polarized Light*, North-Holland, Amsterdam, 1987

[23] W. E. Martin, *Refractive index profile measurements of diffused optical waveguides*, Appl. Opt. 13(9), 2112?2116 (1974).

[24] R. Oven *Extraction of phase derivative data from interferometer images using a continuous wavelet transform to determine two-dimensional refractive index profiles*, Appl. Opt. 49(22), 4228-4236 (2010).

[25] K. S. Chiang *Construction of refractive-index profiles of planar dielectric waveguides from the distribution of effective indexes*, J. Lightwave Technol. 3(2), 385-391 (1985).

[26] W.S. Tsai, S.C. Piao, and P.K. Wei, *Refractive index measurement of optical waveguides using modified end-fire coupling method*, Opt. Lett. 36(11), 2008-2010 (2011).

[27] Catalin Florea, and Kim A. Winick, *Fabrication and Characterization of Photonic Devices Directly Written in Glass Using Femtosecond Laser Pulses*, Journal of Lightwave Technology, Vol. 21, No. 1, January 2003

[28] Alexander Arriola, Simon Gross, Nemanja Jovanovic, Ned Charles, Peter G. Tuthill, Santiago M. Olaizola, Alexander Fuerbach, and Michael J. Withford *Low bend loss waveguides enable compact, efficient 3D photonic chips*, Optics Express, Vol. 21, No. 3, 11 February 2003

[29] Z. Weissman and I. Hendel, *Analysis of Periodically Segmented Waveguide Mode Expanders*, Journal of Lightwave Technology, Vol. 13, No. 10, October 1995